Gravitational collapse in the vicinity of the extremal black hole critical point

William E. East^{1,*}

¹Perimeter Institute for Theoretical Physics, Waterloo, Ontario N2L 2Y5, Canada

We study the threshold of gravitational collapse in spherically symmetric spacetimes governed by the Einstein-Maxwell-Vlasov equations. We numerically construct solutions describing a collapsing distribution of charged matter that either forms a charged black hole or eventually disperses. We first consider a region of parameter space where the solutions at the threshold of black hole formation are stationary, horizonless shells. These solutions terminate at a critical point, with their charge-to-mass ratio approaching unity from below, and the instability timescale diverging. Beyond the critical point, we find a new region of parameter space where the threshold solution is an extremal black hole. We measure the scaling of the dynamical time period of the near threshold solutions and discuss how they are connected in the two regimes. If a similar picture to the one found here holds for known families of stationary solutions of rotating matter that approach the exterior of an extremal Kerr spacetime, they could provide a route to forming an extremal spinning black hole.

I. INTRODUCTION

There is a close analogy between phase transitions and the general relativistic dynamics of gravitational collapse near the threshold of black hole formation. In pioneering work, Choptuik [1] considered different families of collapsing massless scalar field pulses, showing that, approaching threshold, these solutions display universality, self-similarity, and a power law scaling of the black hole mass (above threshold) and the maximum curvature (below threshold) [2]. This is similar to the behavior found in a continuous phase transition at a critical point. The critical solution corresponds to a zero-mass, naked singularity, which means that the cosmic censorship conjecture at best holds with a genericness condition.

Following this, critical phenomena in gravitational collapse has been studied in a number of settings and matter models (see Ref. [3] for a review). This includes the collapse of collisionless particles governed by the Vlasov equation [4–7] (which is the focus of this work), as well as extensions beyond the spherically-symmetric setting originally studied [8–12]. For some matter models and parts of parameter space, the solution at the threshold of black hole formation is a (not necessarily unique) gravitationally bound, but horizonless, star-like solution that is unstable to collapse. In this case, the black hole mass does not become arbitrarily small approaching threshold, and this is usually referred to as "type I," in analogy with a discontinuous phase transition [13, 14] (while cases like that originally studied in Ref. [1] are referred to as type II).

Recently, Kehle and Unger [15] demonstrated a new regime of critical gravitational collapse where the threshold solution is an extremal charged black hole. Building on earlier work studying thin shell [16, 17] or charged null dust [17] models, they mathematically constructed solutions to the Einstein-Maxwell-Vlasov equations corresponding to distributions of charged particles that einstein-Maxwell-Vlasov equations corresponding to distributions of charged particles that

ther eventually disperse, when the total charge exceeds the total mass Q > M (where we use geometric units with G = c = 1 throughout); form a black hole, when Q < M; or form an extremal horizon (with no trapped surfaces) when Q = M. Though the black hole mass does not become arbitrarily small approaching threshold (similar to previously studied type I cases described above, and in contrast to the type II), the threshold solution is continuously connected to the black hole forming cases (in contrast to the usual type I star-like threshold solutions). Such solutions can also be used to construct counter examples to Israel's formulation of third law of black hole mechanics (alongside the charged scalar field construction in Ref. [18]), which states that a black hole cannot have its surface gravity reduced to zero in finite advanced time [19]; here, the black hole's surface gravity corresponds to temperature. An open question raised by this work is, what scaling relations, if any, does extremal critical collapse exhibit near threshold? Another is, can this be extended to the case of an extremal rotating black hole?

In this work, we also study the threshold of black hole formation for collapsing shells of charged matter. We numerically construct solutions of the Einstein-Maxwell-Vlasov equations where, in one regime, the threshold solutions are stationary shell solutions, i.e. a discontinuous phase transition. This behavior terminates at a critical point as Q/M approaches unity below and the compactness of the stationary solutions approaches that of a black hole. Beyond the critical point, we find behavior similar to that in Ref. [15], where the threshold solution is an extremal black hole. We also study how the time for a black hole to form, or for the shell to disperse, scales with how the total charge of the spacetime differs from the threshold value on either side of the critical point. This illuminates how extremal critical collapse is connected to previously studied critical collapse, and deepens the analogy with phase transitions. It also provides a possible route to extending extremal critical collapse to the rotating black hole case, and constructing counter examples to the rotating black hole version of the third law.

 $^{^*}$ weast@perimeterinstitute.ca

II. MODEL AND METHODOLOGY

We evolve the Einstein-Maxwell-Vlasov equations governing a distribution of electrically charged, self-gravitating particles. We restrict to spherically-symmetric spacetimes, and imagine the matter is made up of particles with uniform charge-to-rest-mass ratio q_0 and angular-momentum-magnitude-to-rest-mass ratio $\ell > 0$ (though the stress-energy tensor has no associated angular momentum due to there being no preferred angular direction for the particle velocities). We evolve the metric in ingoing Eddington-Finkelstein-like coordinates

$$ds^2 = -ab^2dt^2 + 2bdtdr + r^2d\Omega^2 , \qquad (1)$$

where t is advanced time, r is the areal radius, and $d\Omega^2$ is the metric on the 2-sphere. The Vlasov equation is evolved using particle-in-cell methods, where we approximate the distribution function using a collection of particles that each follow the Lorentz force equation. The one non-trivial component of the Faraday tensor corresponding to the radial electric field can be determined by integrating over the charge distribution sourced by the particles at each time. Likewise, the metric functions a and b can be determined at each time by integrating matter source terms sourced by the particles. We do this numerically in such a way that, for the outer region of the domain where there are no particles, we obtain exactly (up to floating point roundoff) the Reissner-Nordström solution with specified total mass M and total charge Q. Since a = 1 - 2m(r)/r, where m is the Hawking mass, the presence of an apparent horizon is indicated by a = 0. The explicit equations and the numerical methods used to solve them are given in Appendices A and B.

We consider initial data describing a radially infalling shell of charged particles that is constructed in three steps: (i) we construct a stationary, but unstable solution describing a shell of charged particles where the selfgravity and charge-repulsion balance each other; (ii) we evolve this solution in *outgoing* Eddington-Finkelsteinlike coordinates, letting numerical truncation error excite a linear instability and cause the shell to disperse; (iii) we take the data at some time after the shell has sufficiently dispersed¹, time-reverse it $(t \to -t)$, and apply a perturbation to q_0 and ℓ while keeping the particle positions and radial momentum fixed (and then resolve for the metric and electric field). This procedure then results in data describing an infalling spherical shell which can be evolved in ingoing Eddington-Finkelstein-like coordinates.

The static solutions² used in step (i) are similar to those considered in Ref. [20], consisting of shells with a distribution of radial momenta at each point. In particular, here we choose the distribution function to be

linear in energy, up to some specified maximum energy. Spatially, the particle distribution has non-zero support only within some range $R_{\rm in} < r < R_{\rm out}$. Inside the shell the electric field is zero and the spacetime is flat, and outside the shell the spacetime is the same as Reissner-Nordström. For definiteness, we restrict to static solutions with $q_0 = 1.25$ for the main results, though qualitatively similar results can be obtained for other distribution functions or values of $q_0 > 1$ [20]. (For smaller values q_0 , we do not expect extremal black hole formation [21].) With this choice, the static shell solutions we consider form a one parameter family which can be labelled by the ratio of the total charge Q to total mass M of the spacetime. In particular, we will consider these solutions in the region of parameter space where Q/Mapproaches unity from below. More details on the static solutions and how they are constructed are given in Appendix C. Details on numerical resolution and convergence are given in Appendix D.

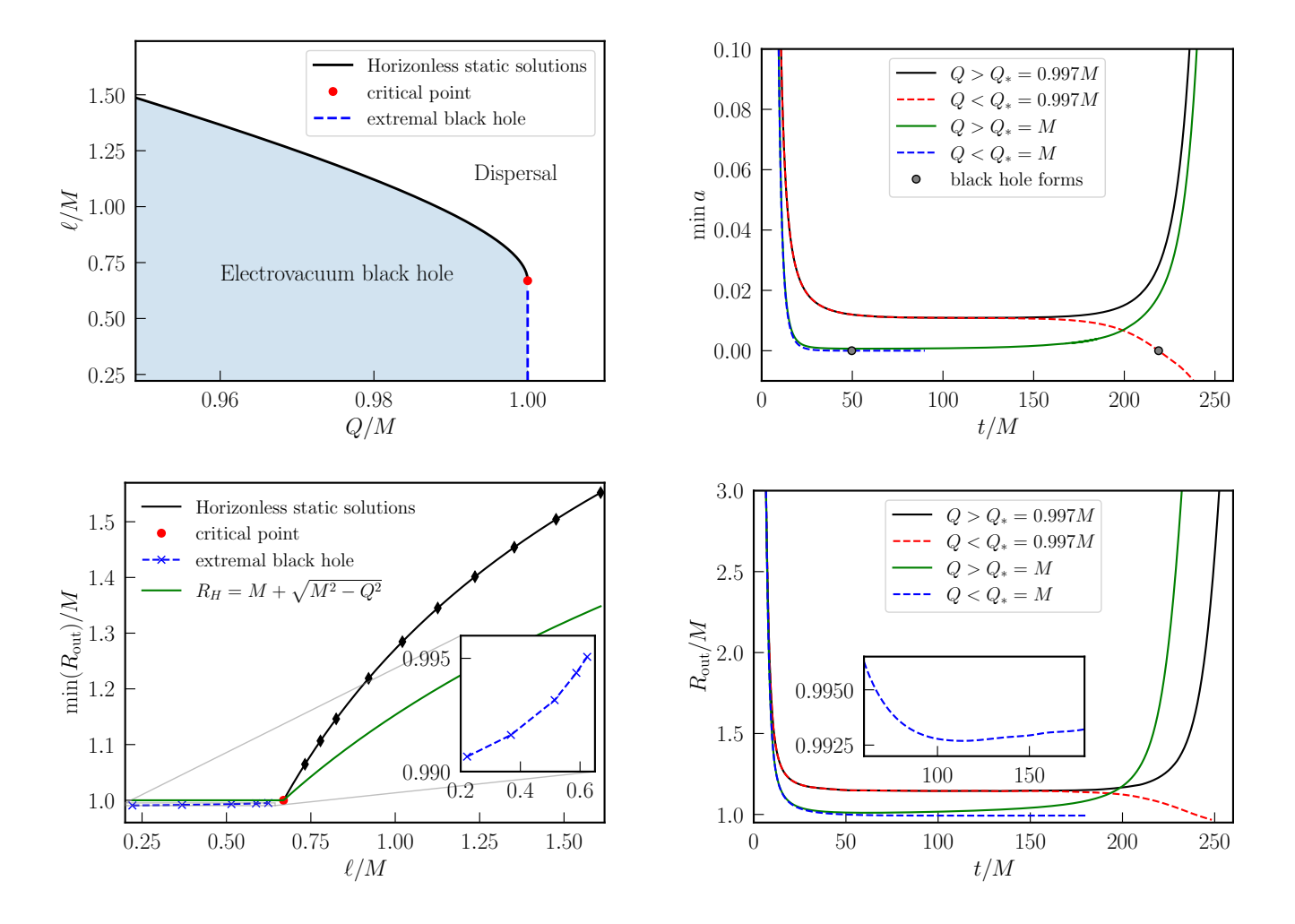
III. RESULTS

Within the considered family of initial data describing an infalling shell of charged matter, we are interested in delineating the boundary between cases where black hole formation does and does not occur. The results we find are summarized by the phase diagram in the top panel of Fig. 1. For larger values of the particle angular momentum ℓ , the boundary of black hole formation corresponds to the unstable, static charged shell solutions indicated by the black line. Solutions with slightly greater charge or particle angular momentum than the static solutions correspond to shells that fall to some radius and then become outgoing, eventually dispersing due to the charge repulsion and angular momentum barrier. Solutions with slightly less charge or angular momentum correspond to infalling shells that form charged black holes, with all the matter falling into the horizon, leaving a Reissner-Nordström exterior solution. For decreasing ℓ approaching some critical value ($\ell_c/M \approx 0.67$ for this case), the charge-to-mass ratio of the static threshold solutions represented by the black curve increases, approaching $Q/M \to 1$ from below. In this limit, the solutions become more and more compact, with the outer radius R_{out} , beyond which the solution is electrovacuum, approaching M (the radius of an extremal black hole) from above. This is shown in the bottom panel of Fig. 1. This limit is singular and the maximum charge density of the static solutions also blows up as $Q/M \to 1$ as these solutions terminate at a critical point (indicated in red).

When we further decrease the value of ℓ/M for the infalling shell solutions below this critical point, we find that the solutions with Q>M eventually fully disperse, while for those with Q< M, all the particles fall into a black hole, with the threshold solution always corresponding to an extremal black hole with Q=M. In the bottom panel of Fig. 1, we show the specific cases

¹ We evolve these solutions until min a = 0.85.

 $^{^2}$ The spacetime is static, though the particles have non-zero velocity.



Top: The phase diagram showing the regions of parameter space that result in a black hole (shaded region) versus those that result in a dispersing charged shell (white region). The x-axis is the total charge of the spacetime (and also the charge of the black hole when it forms) and the y-axis indicates the particle angular momentum. For higher values of the particle angular momentum, the threshold solutions at the boundary between the two regions are static shell solutions (solid black line) which terminate at a critical point (red dot) as $Q/M \to 1$. For lower values, the threshold solution is an extremal black hole (dashed blue line). Bottom: The outer (areal) radius of the threshold solutions, beyond which the spacetime is electrovacuum, as a function the particle angular momentum. For the extremal black hole cases (also shown in the inset), this is the minimum radius the matter reaches inside the horizon. The crosses and diamonds show the specific parameters evolved. The green curve indicates the radius of a Reissner-Nordström black hole with the same charge as the threshold solution.

evolved, as indicated by the marked points. In particular, for the solutions in the vicinity of the static shells solutions, the highest value of Q/M we consider is 0.9994 with $R_{\rm out}/M=1.065$ (i.e. the black diamond closest to the critical point).

FIG. 2. Example evolutions as a function of advanced time just above (solid lines) and below (dashed lines) the threshold for black hole formation in the two regimes, where the threshold solution is either a horizonless shell (black and red curves) or an extremal black hole (blue and green curves). Top: The minimum value of the metric function a(r) = 1 - 2m(r)/r at each time. The circles indicate when a horizon first appears for the dashed lines (a=0). Bottom: The outer radius of the region containing the particles as a function of time. The inset shows a zoom-in to illustrate that $R_{\rm out}$ reaches a minimum slightly below M for the case where $1-Q/M\approx 10^{-12}$.

It is this static solution that we leverage, following the procedure described in the previous section, to construct the initial data for the evolutions where the threshold solution is an extremal black hole, by taking the time reversal of the dispersed unstable static solution and decreasing ℓ while tuning q_0 . In the bottom panel of Fig. 1, we also show the minimum radius (indicated by the blue crosses) that the matter reaches for these cases when an extremal black hole forms (technically, we choose $0 < 1 - Q/M < 10^{-12}$). From there, it can be seen that the electrovacuum region extends a small but

resolved³ amount inside the horizon, min $R_{\rm out} \lesssim 0.995 M$, which increases as ℓ is decreased.

For illustrative purposes, we will now concentrate on two representative cases, corresponding to $\ell \approx 0.825 M >$ ℓ_c (with threshold charge $Q_*/M \approx 0.997$) and $\ell \approx$ $0.515M < \ell_c$ (with threshold charge $Q_*/M = 1$). We show the behavior just above and below the threshold for black hole formation for the two cases in Fig. 2. When the threshold solution is a horizonless static solution (with total charge $Q_* < M$), a near threshold solution corresponds to a shell that fall inwards, spends a long time close to the unstable static solution, and then either disperses when $Q > Q_*$, or collapses further inward and forms a black hole when $Q < Q_*$ (here $|Q/Q_*-1|\sim 10^{-8}$). The advanced time which it takes either to disperse, or to form a black hole (as indicated by an apparent horizon) becomes longer and longer the closer one tunes to the threshold.

When the threshold solution is an extremal black hole $(Q_* = M)$, the time for the shell to fall inward and then disperse when Q > M (we show $Q/M - 1 \approx 10^{-4}$ in Fig. 2) again becomes longer and longer the closer one is to threshold. However, for $Q \leq M$ (we show $1 - Q/M \approx 10^{-12}$ in Fig. 2), the black hole always forms promptly; even for Q = M, R_{out} reaches a minimum value < M before increasing again. The difference above and below threshold is whether a horizon forms which prevents the shell from escaping.

We can measure how these different times scale as one approaches the critical solution. For $Q_* < M$, one expects that both the time for the black hole to form or the time for the shell to disperse (depending on whether one is above or below threshold) should be given by

$$T = -\tau \log |Q - Q_*| + C \tag{2}$$

near threshold, where τ is the e-folding time associated with the linear instability and C is some constant. We indeed find that to be the case, as shown for one example in left panel of Fig. 3. The center panel in Fig. 3 shows how the instability timescale τ varies as one considers more and more compact (but still horizonless) threshold solutions. Approaching the critical point, the instability timescale diverges like

$$\tau \approx M[2(1 - Q_*/M)]^{-1/2} \approx \kappa^{-1}$$
 (3)

where $\kappa = (r_+ - r_-)/(2r_+)$ with $r_{\pm} = M \pm \sqrt{M^2 - Q^2}$ is the surface gravity, and the approximation holds to leading order in the extremal limit.

Now considering the case where the threshold solution is an extremal black hole $(Q_* = M)$, we can measure

the time for the solution to eventually disperse as Q approaches M from above. We show this in the right panel of Fig. 3. We find that this time also scales like

$$T \sim M(Q/M - 1)^{-1/2}$$
 (4)

In this sense, the exponents governing the dispersal time on either side of the critical point match (though the scaling of the time for black hole formation does not).

The above scaling can also be derived by considering the orbits of a charged test particle near the horizon of a near-extremal Reissner-Nordström black hole. When $q_0 > \sqrt{\ell^2 + 1}$, there are circular orbits at radii approaching the horizon as $Q/M \to 1$; these are unstable with a Lyapunov timescale that has the scaling [22] $\lambda_{RN} \approx \kappa$ in this limit. That is, a small perturbation to the radius of the circular orbit radius grows likes $\delta r = \delta r(t=0)e^{\lambda t}$. Roughly, we can think of the outer edge of the charged shell as behaving in a similar way to such particle orbits. (Though note that the stationary spherical shell solutions have a distribution of radial velocities.) Now letting Qapproach M from above, if we consider the advanced time it will take a null geodesic to go from some fixed initial radius < M to some fixed large radius $\gg M$ in near but super-extremal Reissner-Nordström, which gives an upper bound on the time for a timelike trajectory, we likewise obtain a scaling like Eq. 4.

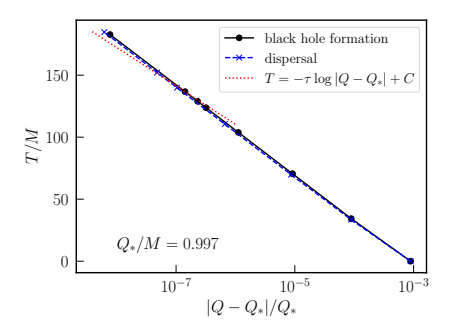
IV. EXTENDING TO SPINNING BLACK HOLES

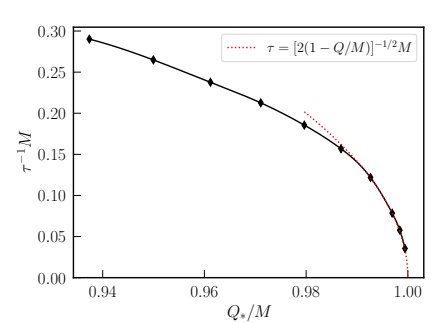
We now briefly discuss how the picture found here for charged black holes might be extended to spinning black holes. Beginning with the work of Ref. [23], there have been several studies constructing stationary, axisymmetric solutions of uniformly rotating dust [24] or a fluid with pressure [25, 26], demonstrating families of solutions where the matter velocity becomes ultrarelativistic, while the total angular momentum approaches extremality $J \to M^2$ and the spacetime approaches the exterior of extremal Kerr. In this limit, the matter distribution becomes a thin ring concentrated near the equatorial plane. However, the stability or instability of these solutions has not been explored. Timelike, circular geodesics in the equator of Kerr are unstable for radii approaching the photon ring, suggesting that the ring solutions will be similarly unstable approaching the critical point. For a circular, equatorial null geodesic in Kerr, approaching extremality, the Lyapunov exponent is given by

$$\lambda/\omega_0 \approx (2M\kappa) \approx 2^{1/2} (1 - J/M^2)^{1/2}$$
 (5)

where we have normalized by the orbital frequency of the null geodesic (e.g., Ref. [27]). Thus, we can conjecture that these ring solutions would be subject to an instability where small perturbations would cause them to collapse to a Kerr black hole, or disperse, but that the associated instability timescale would become longer

 $^{^3}$ We estimate that $\min R_{\rm out}$ is accurate to better than 0.1%, and that finite resolution actually leads to an overestimate. See Appendix D.





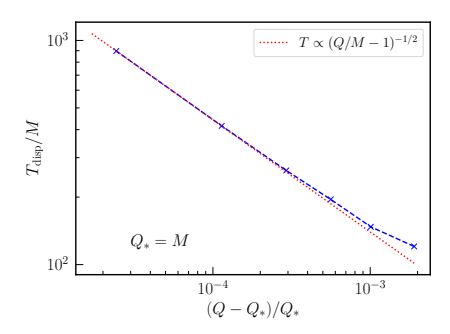


FIG. 3. Timescales governing near threshold behavior above (left and center panels) and below (right) the critical particle angular momentum ℓ_c . Left: The time it takes for a black hole apparent horizon to form (black) or for the charged shell to disperse (blue; defined as $R_{\rm out}/M=10$) as a function of the difference in the total charge from its threshold value. Time is measured as the difference in the ingoing Eddington-Finkelstein coordinate from when this occurs when $|1-Q/Q_*|=10^{-3}$. This approximately matches the dependence expected from measuring the instability timescale of the static threshold solution (dashed red curve). Center: The inverse instability timescale (i.e. instability rate) for the static charged shell solutions, as a function of their total charge. The dotted red line shows an analytic prediction from the surface gravity of a near extremal black hole with the same mass and spin. Right: The time it takes for the charged shell to disperse (defined as $R_{\rm out}/M=10$) as a function of how much the total charge is above the threshold value of $Q_*=M$ (for $\ell/M\approx 0.52$). This matches well with a -1/2 power law scaling (dotted red line).

and longer as $J \to M^2$ with the above scaling. Following a similar procedure to one used above to extend beyond the critical point might then be a way to construct solutions describing an infalling ring of rotating matter that forms an extremal Kerr black hole in finite time. One possible complication to this picture is that even restricting to axisymmetry there would be gravitational radiation. (Further, allowing non-axisymmetric perturbations would open up the possibility of new instabilities, like the ergoregion instability [28].)

V. DISCUSSION AND CONCLUSION

In this work, we have studied the threshold of the formation of a black hole with large charge in the Einstein-Maxwell-Vlasov model. We find a phase diagram where extremal black hole formation emerges as the threshold solution when extending beyond the critical point marking the end of a discontinuous (type I) transition where the threshold solution is a stationary charged shell. In the latter regime, the lifetime of the intermediate stationary shell solution scales logarithmically with the difference of the total charge from its threshold value, approaching $T \sim \kappa^{-1} \log |Q - Q_*|$, where κ is the surface gravity of the black hole that forms around threshold.

Beyond the critical point, in the regime where the threshold solution is an extremal charged black hole, the dispersal time exhibits a $\sim |1-Q/M|^{-1/2}$ scaling (in advanced time) when a black hole does not form, though when a black hole does form, it forms promptly. In this regime, black hole formation switches on at zero surface gravity (though at non-zero mass/horizon area), and above or below threshold, the solutions correspond to

charged shells that fall to some minimum radius and then expand outwards. The sharp distinction is just whether or not the matter eventually disperses to the asymptotic region, or is instead confined behind the black hole horizon.

The above picture shares some characteristics with canonical examples of phase transitions, like the liquid-vapor transition, where a discontinuous (type I) phase transition terminates at a critical pressure and temperature. Approaching the critical point, the jump in, e.g., density, across the phase transition goes to zero. At the critical point the transition is continuous (type II); beyond this there is a supercritical fluid without a sharp phase distinction.

By leveraging stationary solutions, we have found an alternative route, from that of Ref. [15], to constructing dynamical solutions where an extremal black hole forms in finite time. In future work, it would be particularly interesting to determine if stationary solutions describing rotating rings of matter [23–26] could likewise be leveraged to construct dynamical solutions describing critical collapse with an extremal Kerr black hole as the threshold solution, as well as counter examples to the third law of black hole mechanics for rotating black holes. Based on test particle orbits, we speculate that the scaling will be the same in the rotating and charged extremal critical collapse cases. In Ref. [29], this same scaling was also arrived at by invoking quasinormal modes in the near extremal Kerr limit.

ACKNOWLEDGMENTS

The author thanks Patrick Brady, Christoph Kehle, and Ryan Unger for useful discussions. The author acknowledges support from a Natural Sciences and Engineering Research Council of Canada Discovery Grant and an Ontario Ministry of Colleges and Universities Early Researcher Award. Research at Perimeter Institute is supported in part by the Government of Canada

through the Department of Innovation, Science and Economic Development Canada and by the Province of Ontario through the Ministry of Colleges and Universities. This research was enabled in part by support provided by SciNet (www.scinethpc.ca) and the Digital Research Alliance of Canada (www.alliancecan.ca). Simulations were performed on the Symmetry cluster at Perimeter Institute and the Trillum cluster at the University of Toronto.

- [1] M. W. Choptuik, Phys. Rev. Lett. 70, 9 (1993).
- [2] D. Garfinkle and G. C. Duncan, Phys. Rev. D 58, 064024 (1998), arXiv:gr-qc/9802061.
- [3] C. Gundlach, D. Hilditch, and J. M. Martín-García, (2025), arXiv:2507.07636 [gr-qc].
- [4] G. Rein, A. D. Rendall, and J. Schaeffer, Phys. Rev. D 58, 044007 (1998), arXiv:gr-qc/9804040.
- [5] I. Olabarrieta and M. W. Choptuik, Phys. Rev. D 65, 024007 (2002), arXiv:gr-qc/0107076.
- [6] J. M. Martin-Garcia and C. Gundlach, Phys. Rev. D 65, 084026 (2002), arXiv:gr-qc/0112009.
- [7] A. Akbarian and M. W. Choptuik, Phys. Rev. D 90, 104023 (2014), arXiv:1409.5176 [gr-qc].
- [8] A. M. Abrahams and C. R. Evans, Phys. Rev. Lett. 70, 2980 (1993).
- [9] M. W. Choptuik, E. W. Hirschmann, S. L. Liebling, and F. Pretorius, Phys. Rev. D 68, 044007 (2003), arXiv:gr-qc/0305003.
- [10] T. W. Baumgarte, C. Gundlach, and D. Hilditch, Phys. Rev. Lett. 123, 171103 (2019), arXiv:1909.00850 [gr-qc].
- [11] T. W. Baumgarte, B. Brügmann, D. Cors, C. Gundlach, D. Hilditch, A. Khirnov, T. Ledvinka, S. Renkhoff, and I. S. Fernández, Phys. Rev. Lett. 131, 181401 (2023), arXiv:2305.17171 [gr-qc].
- [12] K. Marouda, D. Cors, H. R. Rüter, A. Vaño-Viñuales, and D. Hilditch, (2025), arXiv:2511.04649 [gr-qc].
- [13] M. W. Choptuik, T. Chmaj, and P. Bizon, Phys. Rev. Lett. **77**, 424 (1996), arXiv:gr-qc/9603051.
- [14] P. R. Brady, C. M. Chambers, and S. M. C. V. Goncalves, Phys. Rev. D 56, R6057 (1997), arXiv:gr-qc/9709014.
- [15] C. Kehle and R. Unger, (2024), arXiv:2402.10190 [gr-qc].
- [16] M. Proszynski, General Relativity and Gravitation 15, 403 (1983).
- [17] A. Ori, Classical and Quantum Gravity 8, 1559 (1991).
- [18] C. Kehle and R. Unger, (2022), arXiv:2211.15742 [gr-qc].
- [19] W. Israel, Phys. Rev. Lett. 57, 397 (1986).
- [20] H. Andreasson, M. Eklund, and G. Rein, Class. Quant. Grav. 26, 145003 (2009), arXiv:0903.4092 [gr-qc].
- [21] H. S. Reall, Phys. Rev. D 110, 124059 (2024), arXiv:2410.11956 [gr-qc].
- [22] N. Kan and B. Gwak, Phys. Rev. D 105, 026006 (2022), arXiv:2109.07341 [gr-qc].
- [23] J. M. Bardeen and R. V. Wagoner, Astrophys. J. 167, 359 (1971).
- [24] G. Neugebauer and R. Meinel, Phys. Rev. Lett. 75, 3046 (1995), arXiv:gr-qc/0302060.
- [25] M. Ansorg, A. Kleinwachter, and R. Meinel, Astrophys. J. Lett. 582, L87 (2003), arXiv:gr-qc/0211040.

- [26] T. Fischer, S. Horatschek, and M. Ansorg, Mon. Not. Roy. Astron. Soc. 364, 943 (2005), arXiv:gr-qc/0506105.
- [27] F. Pretorius and D. Khurana, Class. Quant. Grav. 24, S83 (2007), arXiv:gr-qc/0702084.
- [28] J. L. Friedman, Commun. Math. Phys. 63, 243 (1978).
- [29] H. Yang and L. Zou, Phys. Rev. D 109, 104034 (2024), arXiv:2207.04373 [gr-qc].
- [30] H. Andreasson and G. Rein, J. Hyperbol. Diff. Equat. 7, 707 (2010), arXiv:0910.1254 [gr-qc].

Appendix A: Evolution Equations

We evolve the Einstein-Maxwell-Vlasov equations governing a distribution of electrically charged and self-gravitating particles with charge \mathfrak{e} and rest mass \mathfrak{m} . The Vlasov equation describing the evolution of the distribution function $f(t, x^i, p^i)$ for the particles is given by

$$\frac{\partial f}{\partial t} + \frac{p^i}{p^t} \frac{\partial f}{\partial x^i} - \frac{1}{p^t} \left(\Gamma^i_{ab} p^a p^b + \mathfrak{e} p^a F_a{}^i \right) \frac{\partial f}{\partial p^i} = 0 \ , \quad (A1)$$

where F_{ab} is the Faraday tensor, Γ^a_{bc} is the Christoffel symbol, and the index i runs over spatial indices. The four momentum of the particle $p^a = (p^t, p^i)$ satisfies the normalization condition $p_a p^a = -\mathfrak{m}^2$. The contribution to the stress-energy tensor is then given by

$$T_{ab} = -\int p_a p_b f \sqrt{-g} \frac{d^3 p}{p_t} , \qquad (A2)$$

while the current sourced by this matter is

$$J^a = -\mathfrak{e} \int p^a f \sqrt{-g} \frac{d^3 p}{p_t}.$$
 (A3)

The Maxwell equations are

$$\nabla_b F^{ab} = 4\pi J^a \text{ and } \nabla_{[a} F_{bc]} = 0, \tag{A4}$$

and the electromagnetic field contributes to the stress-energy tensor as

$$T_{ab}^{\text{EM}} = \frac{1}{4\pi} \left(F_a{}^c F_{bc} - \frac{1}{4} g_{ab} F_{cd} F^{cd} \right) .$$
 (A5)

The Einstein equations (in terms of the Einstein tensor) are then

$$G_{ab} = 8\pi (T_{ab} + T_{ab}^{\text{EM}}).$$
 (A6)

We assume a spherically symmetric spacetime and use Eddington-Finkelstein-like coordinates (e.g., Ref. [30]) where the line element is given by

$$ds^2 = -ab^2dt^2 + 2bdtdr + r^2d\Omega^2 . (A7)$$

Here r is the areal radius. There is one independent component to the Faraday tensor which can be found from

$$\partial_r q = 4\pi r^2 \rho_a \,, \tag{A8}$$

where $q := |b|r^2 F^{tr}$ is the total charge enclosed within a given radius, and $\rho_q := bJ^t$ is the charge density. The metric functions are determined by

$$\partial_r \log |b| = 4\pi r T_{rr} \tag{A9}$$

and

$$a = 1 - \frac{2m}{r},\tag{A10}$$

where

$$\frac{1}{b}\partial_r(mb) = 2\pi r^2 (T_{rr} + S) + \frac{q^2}{2r^2}.$$
 (A11)

Here we have defined

$$S = \frac{-2}{b}T_{tr} - aT_{rr} . (A12)$$

For r = 0, q = 0, m = 0, and a = 1. As $r \to \infty$, $q \to Q$, $m \to M$, $a \to 1$ and $b \to \pm 1$ (for ingoing or outgoing, respectively).

In these coördinates, the Lorentz force equation for a particle with rest mass \mathfrak{m} , charge \mathfrak{e} , and angular momentum squared $\mathfrak{l}^2 = p_{\Omega}^2$ takes the form

$$\begin{split} \frac{dr}{dt} &= \frac{1}{2}ab - \frac{b}{2p_r^2}(\mathfrak{m}^2 + \mathfrak{l}^2/r^2), \qquad \text{(A13a)} \\ \frac{dp_r}{dt} &= -\frac{p_r}{2}\left(a\partial_r b + b\partial_r a\right) - \frac{\partial_r b}{2p_r}(\mathfrak{m}^2 + \mathfrak{l}^2/r^2) \\ &+ \frac{b\mathfrak{l}^2}{p_r r^3} + \frac{\mathfrak{e}|b|q}{r^2}. \qquad \text{(A13b)} \end{split}$$

In all cases here, we consider a distribution of particles with fixed charge to rest mass ratio $q_0 = \mathfrak{e}/\mathfrak{m}$ and angular momentum magnitude to rest mass ratio $\ell = \mathfrak{l}/\mathfrak{m}$.

Appendix B: Numerical methods

We numerically evolve the Einstein-Maxwell-Vlasov equations using particle-in-cell methods. We use N particles to approximate the distribution function, together with a numerical grid that is regularly space in the compactified radial coordinate $\bar{r} := r/(1+r)$, where the domain is given by $\bar{r} \in [0,1]$; that is, the grid extends to spatial infinity. For each particle, we evolve the radial position r and radial momentum p_r by integrating

Eq. (A13) using fourth-order Runge-Kutta. The time component of the particle four momentum is determined through the normalization condition $p_a p^a = -\mathfrak{m}^2$. The fields a, b, their radial derivatives, and q are interpolated to the particle positions using linear interpolation.

To determine q, b, and a at the grid points, we numerically integrate Eqs. (A8), (A9), and (A11) using extended Newton-Cotes, a fourth order accurate integration scheme. The particle source terms are calculated by having each particle contribute a fraction to the two vertices it lies between, weighted linearly by its distance to each. Explicitly, the sources are given by summing over all particles as

$$\rho_q(\bar{r}) = \sum_{n=1}^{N} w(\bar{r}, \bar{r}_n) \frac{\mathfrak{e}}{\Delta V(r_n)} , \qquad (B1a)$$

$$T_{rr}(\bar{r}) = \sum_{n=1}^{N} w(\bar{r}, \bar{r}_n) \frac{(p_r)_n}{\Delta V(r_n)},$$
 (B1b)

$$S(\bar{r}) = \sum_{n=1}^{N} w(\bar{r}, \bar{r}_n) \frac{\mathfrak{m}^2 + \mathfrak{l}^2 / r_n^2}{\Delta V(r_n) (p_r)_n} .$$
 (B1c)

Here $\Delta V = (4\pi/3)(r_{i+1}^3 - r_i^3)$ is the coordinate volume of the grid cell the particle lies in $(r_i < r_n < r_{i+1})$, and

$$w(\bar{r}, \bar{r}_p) = \begin{cases} |1 - (\bar{r} - \bar{r}_p)/\Delta \bar{r}| & \text{if } |\bar{r} - \bar{r}_p| < \Delta \bar{r} \\ 0 & \text{otherwise} \end{cases}$$
(B2)

is a weight function that is linear in the compactified coordinate distance from the particle position \bar{r}_p with compact support over twice the width of one grid cell $\Delta \bar{r}$. Radial derivatives of a and b are solved for directly using Eqs. (A9) and (A11).

Equation (A9) can integrated from spatial infinity to give

$$b = \pm \exp(-4\pi \int_{r}^{\infty} r' T_{rr} dr') , \qquad (B3)$$

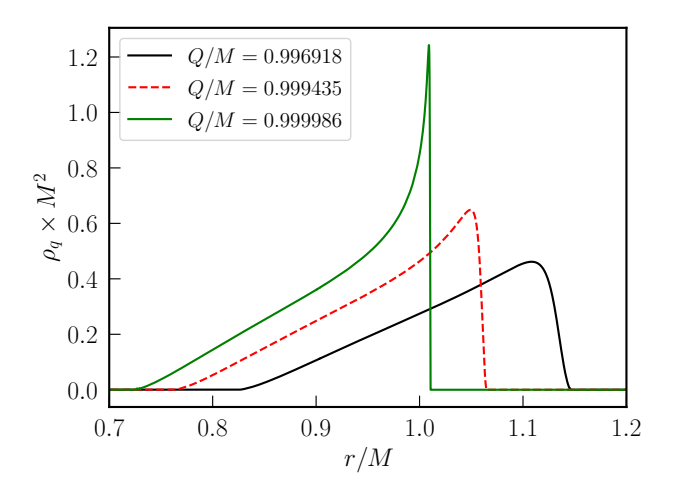
where the plus (minus) sign refers to ingoing (outgoing) coördinates. When using outgoing coördinates, we integrate Eqs. (A8) and (A11) beginning from r = 0, where q = 0 and a = 1 (m = 0).

When using ingoing coördinates, where a black hole interior may be included in the domain, we fix the total charge Q and total spacetime mass M at t=0, and integrate Eqs. (A8) and (A11) from spatial infinity. Explicitly, we solve

$$q = Q - \int_{r}^{\infty} \rho_q dr' \tag{B4}$$

and

$$mb = M - \frac{Q^2}{2r} - \int_r^{\infty} \left(2\pi b r'^2 (T_{rr} + S) + \frac{bq^2 - Q^2}{2r'^2} \right) dr'$$
(B5)



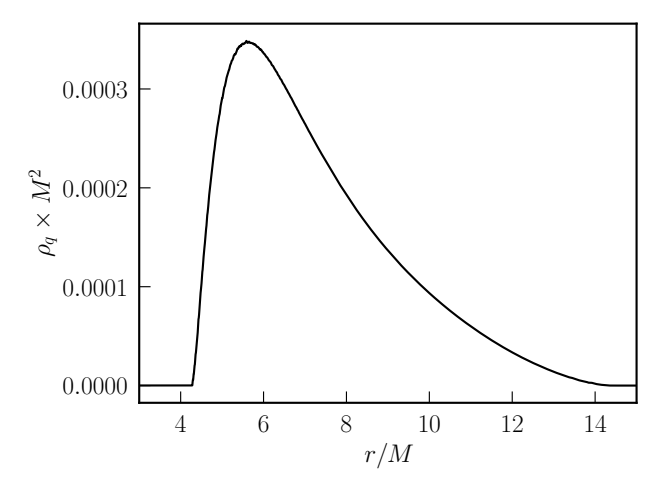


FIG. 4. Charge density as function of areal radius. Top: Several static shell solutions approaching $Q/M \to 1$. Bottom: Charge density obtained after letting the intermediate case in the top panel disperse. This is used for initial data for the evolutions where the threshold solution is an extremal black hole.

where the integrals are approximated numerically. Note that, with this scheme, the outer region $r > R_{\rm out}$ where there are no particles, and hence the above integrands vanish, will be exactly Reissner-Nordström (with no truncation error), i.e.

$$q(r > R_{\text{out}}) = Q$$
, (B6a)

$$b(r > R_{\text{out}}) = 1$$
, (B6b)

$$a(r > R_{\text{out}}) = 1 - \frac{2M}{r} + \frac{Q^2}{r^2}$$
 (B6c)

Appendix C: Constructing static solutions

Here we give more details on constructing static, spherically symmetric solutions to the Einstein-Maxwell-Vlasov equations following Ref. [20]. Using the Killing

vector \hat{t}^a associated with stationarity, the conserved particle energy (per rest-mass) is

$$E = -\frac{1}{m}\hat{t}^a(p_a + \mathfrak{e}A_a) , \qquad (C1)$$

where A_a is the vector potential satisfying

$$F_{ab} = \nabla_a A_b - \nabla_b A_a , \qquad (C2)$$

and we will choose $\hat{t}^a A_a = 0$ at r = 0. A distribution function that only depends on the particle energy and angular momentum automatically satisfies the static Vlasov equation. We use a slight simplification of the solutions constructed in Ref. [20] and consider a distribution function that is a linear function of energy up to some maximum value E_0 , with a single allowed value of angular momentum

$$f(E,\ell) \propto \begin{cases} (1 - E/E_0)\delta(\ell - \ell_0) & \text{if } E < E_0 \\ 0 & \text{otherwise} \end{cases}$$
 (C3)

We solve for the static solution in Schwarzschild coordinates:

$$ds^{2} = -e^{2\mu}d\tilde{t}^{2} + e^{2\lambda}dr^{2} + r^{2}d\Omega^{2} . \tag{C4}$$

After fixing ℓ_0 and q_0 , one obtains a family of solutions by choosing different values of $e^{2\mu}/E_0^2$ at r=0 and then integrating the ordinary differential equations determining the electric field and metric (see Ref. [20]). These solutions are shell-like in that the matter is zero for $r < R_{\rm in}$ with

$$R_{\rm in} = \ell_0 \left[E_0^2 e^{-2\mu} (r=0) - 1 \right]^{-1/2}$$
 (C5)

and also zero for $r>R_{\rm out}$ for finite $R_{\rm out}$, where the solution is Reissner-Nordström.

In order to evolve these solutions, we perform a coordinate transformation to outgoing coördinates:

$$t = \tilde{t} - \int_0^r e^{\lambda - \mu} dr' \tag{C6}$$

which gives $a = e^{-2\lambda}$ and $b = -e^{\lambda+\mu}$. To approximate the initial distribution function, we use $N = N_r \times N_p$ particles placed at different radii $\{r_i\}$ with $i = 1, \ldots, N_r$ defined (in terms of the floor function) by

$$i = |N_r q(r_i)/Q + 1/2|,$$
 (C7)

where at each position there are N_p particles with different values of the radial momentum $\{p_r^j\}$ given by

$$j = |N_p P(r_i, p_r^j)/P(r_i, p_r^{\text{max}}) + 1/2|,$$
 (C8)

with

$$P(r, p_r) := \int_{p_{\min}}^{p_r} \left[1 - E(r, p_r') / E_0 \right] dp_r'.$$
 (C9)

The limits p_r^{\min} and p_r^{\max} are, respectively, the minimum and maximum values compatible with $E = E_0$.

In the top panel of Fig. 4, we show the charge density for several of the static shell solutions with $q_0 = 1.25$ approaching $Q/M \to 1$. The intermediate value of Q/M shown there is the highest value that we use when following the dispersal of one of these static solutions. As described above, we evolve the static solutions until they sufficiently disperse, and then adjust ℓ and q_0 and use the time reversal as initial data. An example of the charge density profile from initial data constructed this way is shown in the bottom panel of Fig. 4.

Appendix D: Convergence results

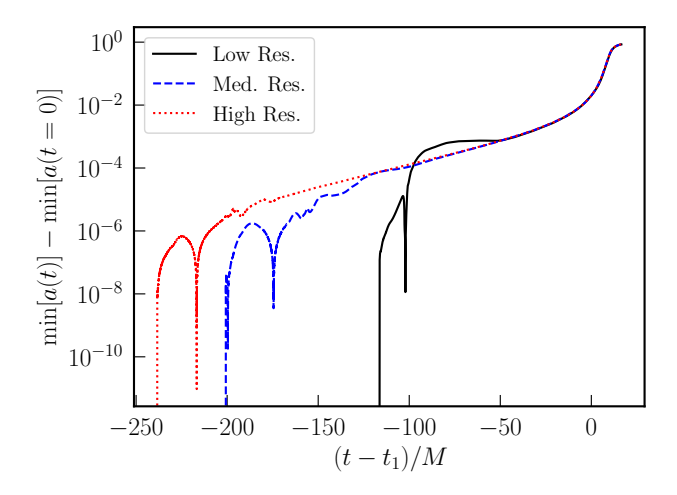


FIG. 5. Resolution study of an unstable static solution (with $Q/M \approx 0.9994$) dispersing when evolved in outgoing coordinates. We show the difference in the minimum value of the metric function a from its initial value. The times have been shifted to align the curves when $\min(a) = 0.02$

The numerical grid we use is uniformly spaced in the compactified coördinate $\bar{r} \in [0,1]$. For most of the results we present in this study, we use a grid spacing of $\Delta \bar{r} = 1/12288$, along with $N_r = 18432$ and $N_p = 1536$ for a total of $N \approx 2.8 \times 10^7$ particles. For select cases, we repeat the computation with lower and higher resolution where the grid spacing is, respectively, $1.5\Delta \bar{r}$ and

 $0.75\Delta\bar{r}$, and we use $(2/3)^3N$ and $(4/3)^3N$ particles. In Fig. 5, we show a resolution study of a static solution near the critical point dispersing, due to just truncation error exciting an exponentially growing mode. As expected, as the resolution is increased, the unstable mode is seeded at a smaller and smaller amplitude. In Fig. 6, we show a comparison of the outer radius of the particles as a function of time for incoming shell cases above, and just below the threshold for formation of an extremal black hole, each at the three different resolutions. (For the

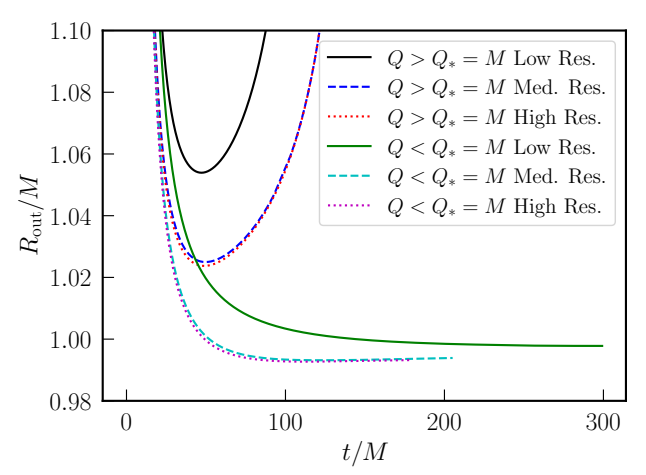


FIG. 6. Resolution study of two cases, above and below the threshold for the formation of an extremal black hole, each at three different numerical resolutions. We show the outer radius, beyond which the solution is electrovacuum, as a function of advanced time, around when it reaches a minimum.

case where a black hole forms, it is essentially extremal: $Q/M-1\approx 10^{-12}$.) We can see that finite resolution leads to an overestimate of the minimum outer radius of the particles. For Q>M, the difference between the medium and high resolutions in $\min(R_{\rm out})$ is $\sim 0.1\%$, while for the Q< M case it is 0.05%. Though evaluating the overall truncation error is somewhat complicated by the fact that it depends on both the number of grid points and particles, we roughly find the convergence in this quantity to be consistent with fourth order in the grid spacing, and estimate the error in $\min(R_{\rm out})$ for the highest resolution to be a factor of a few smaller than the difference between the medium and high resolution.